Int. J. Heat Mass Transfer. Vol. 30, No. 11, pp. 2289–2303, 1987
Printed in Great Britain

0017–9310/87 $3.00 + 0.00

The horizontal spreading of thermal and chemical deposits in a porous medium

ZONGQIN ZHANG and ADRIAN BEJAN
Department of Mechanical Engineering and Materials Science, Duke University, Durham, NC 27706, U.S.A.

(*Received* 19 *January* 1987 *and in final form* 5 *April* 1987)

Abstract—This is an analytical and numerical study of the buoyancy-driven horizontal spreading of heat and chemical species through a fluid-saturated porous medium. The buoyancy effect is due to both temperature and concentration gradients. It is shown that when the flow is driven primarily by temperature gradients the approach to eventual thermal equilibrium can take place along two distinct routes, one dominated by convection (high Ra) effects, and the other dominated by diffusion. In the convection dominated regime, for example, the porous medium reaches an intermediate state of stable stratification (horizontal layering) before the final state of uniform temperature. It is shown also that the species migration processes that ride on flows driven by temperature gradients can be sorted out similarly, depending on whether mass convection is important. The scaling trends and estimates discovered analytically are confirmed by extensive numerical experiments conducted in the range $10 < Ra < 10^3$, $0.01 < Le < 100$ and $1 < L/H < 4$. The distinct regimes and respective heat and mass transfer scales of the flows driven primarily by buoyancy due to concentration gradients are also documented. A closed form analytical solution is developed for the limit of infinitely shallow layers, $L/H \to \infty$.

1. INTRODUCTION

ONE OF the most important applications of the study of natural convection in fluid-saturated porous media is in the engineering of effective methods for the disposal of waste material (thermal, nuclear, chemical). This application was illustrated early by Hickox and Watts [1] who developed numerical solutions for the field affected by a point heat source, when convection plays a dominant role. In a subsequent paper Hickox [2] showed that the transient and steady state solutions to the small-Ra point source can be superimposed in order to predict the flow and temperature field around buried objects of more complicated geometries. The more general problem of buoyancy-driven dispersion of heat and mass from a buried source was considered very recently by Poulikakos [3, 4].

Our objective in the present study is to become able to predict the spreading rate and time scale of a large finite-size region that, relative to the rest of the porous medium, has been contaminated by the deposition of both thermal and chemical waste. This is a most basic problem the counterpart of which in the field of 'pure fluid' fluid mechanics has attracted considerable attention. One modern application of the pure-fluid version of the problem was demonstrated recently by Scott *et al.* [5], in a wide ranging study of the transient heat transfer between two adjacent enclosures communicating in the horizontal direction. Another application of the porous-medium version of the problem concerns the subsurface migration of a chemical species.

2. MATHEMATICAL FORMULATION

Consider the two-dimensional rectangular porous medium sketched in Fig. 1, where the four sides are assumed adiabatic and impermeable. The fluid mixture that saturates the porous medium is such that the two halves (left and right) of the system are initially at different temperatures (T_1 and T_0) and different concentrations of a certain constituent (C_1 and C_0). The concentration C represents the number of kilograms of constituent per unit volume of fluid saturated porous medium.

In accordance with the Darcy flow model and the homogeneous porous medium model, the conservation equations for mass momentum, energy and constituent are [6–8]

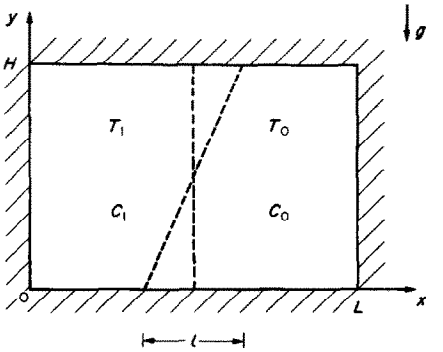

FIG. 1. Two-dimensional isolated porous medium, with initial temperature and concentration differences present in the horizontal direction.

NOMENCLATURE

c	specific heat [J kg^{-1} K^{-1}]
c_P	specific heat at constant pressure [J kg^{-1} K^{-1}]
C	concentration of chemical species [kg m^{-3}]
C_0, C_1	initial concentrations, Fig. 1
ΔC	concentration difference, $C_1 - C_0$ [kg m^{-3}]
D	mass diffusivity [m^2 s^{-1}]
f_0, f_1	functions, equations (55) and (57)
g	gravitational acceleration [m s^{-2}]
H	height [m]
K	permeability [m^2]
l	horizontal displacement of the T_1/T_0 interface in heat-transfer-driven flows [m]
l_C	horizontal displacement of the C_1/C_0 interface in heat-transfer-driven flows [m]
l_m	horizontal displacement of the C_1/C_0 interface in mass-transfer-driven flows [m]
l_T	horizontal displacement of the T_1/T_0 interface in mass-transfer-driven flows [m]
L	horizontal length [m]
Le	Lewis number, α/D
N	buoyancy ratio, equation (20)
P	pressure [Pa]
q	heat transfer rate per unit length [W m^{-1}]
q_0	heat transfer rate due to secondary flow driven by diffusion, equation (49)
q_1	horizontal convective heat transfer rate, equation (48)
Ra	Darcy–modified Rayleigh number, equation (20)
Ra_m	Darcy–Rayleigh number for mass-transfer-driven flows, equation (73)
t	time [s]
t_1, t_2, t_3, t_4, t_5	time scales defined in equations (37), (38), (62), (64) and (68), respectively
$(t_1, t_2, t_3, t_4, t_5)_m$	corresponding time scales of mass-transfer-driven flows, equations (74), (76) and (78)
$\hat{t}_0$	time of vertical boundary layer development, equation (44)
t_{C90}	time scale of the end of horizontal mass transfer [s]
t_{T90}	time scale of the end of horizontal heat transfer [s]
T	temperature [K]
T_0, T_1	initial temperatures, Fig. 1
ΔT	temperature difference, $T_1 - T_0$ [K]
u, v	horizontal and vertical velocity components [m s^{-1}]
u_0, v_0	velocity scales defined in equations (46) and (47)
u_1, v_1	velocity scales defined in equations (33) and (34)
x, y	horizontal and vertical coordinates [m].

Greek symbols

α	thermal diffusivity [m^2 s^{-1}]
β	coefficient of thermal expansion [K^{-1}]
β_c	concentration expansion coefficient [m^3 kg^{-1}]
δ	thermal penetration distance [m]
δ_0	final thickness of vertical boundary layer, equation (45)
μ	viscosity [kg m^{-1} s^{-1}]
ν	kinematic viscosity [m^2 s^{-1}]
ρ	density [kg m^{-3}]
σ	heat capacity ratio, equation (6)
ϕ	porosity
ψ	streamfunction [m^2 s^{-1}].

Subscripts

$()_f$	fluid
$()_m$	scales of mass-transfer-driven flows
$()_s$	solid.

Superscripts

$\hat{()}$	dimensionless variables used in numerical experiments (Section 3)
$\tilde{()}$	dimensionless variables used in the $L/H \to \infty$ asymptotic solution (Section 6).

$$\frac{\partial u}{\partial x} + \frac{\partial v}{\partial y} = 0 \tag{1}$$

$$u = -\frac{K}{\mu}\frac{\partial P}{\partial x}, \quad v = -\frac{K}{\mu}\left(\frac{\partial P}{\partial y} + \rho g\right) \tag{2,3}$$

$$\sigma\frac{\partial T}{\partial t} + u\frac{\partial T}{\partial x} + v\frac{\partial T}{\partial y} = \alpha\left(\frac{\partial^2 T}{\partial x^2} + \frac{\partial^2 T}{\partial y^2}\right) \tag{4}$$

$$\phi\frac{\partial C}{\partial t} + u\frac{\partial C}{\partial x} + v\frac{\partial C}{\partial y} = D\left(\frac{\partial^2 C}{\partial x^2} + \frac{\partial^2 C}{\partial y^2}\right) \tag{5}$$

where u, v, x, y, P, T and C are the volume-averaged velocity components, the Cartesian coordinates, the pressure, the temperature and the concentration. The symbols μ, ρ and α represent the fluid viscosity, the fluid density and the thermal diffusivity of the fluid-

saturated porous medium (fluid+solid) divided by the specific heat capacity of the fluid phase alone. The effect of thermal dispersion is being neglected. Parameters K, ϕ and D are the permeability, the porosity and the effective mass diffusivity of the constituent as it diffuses through the mixture-saturated porous medium. Parameter σ is the heat capacity ratio

$$\sigma = \phi + (1-\phi)\frac{(\rho c)_s}{(\rho c_p)_f} \tag{6}$$

where $(\rho c)_s$ is the specific heat capacity of the solid matrix. In the limit of sufficiently small temperature and concentration differences, the momentum equations, equations (2) and (3), combine into

$$\frac{\partial u}{\partial y} - \frac{\partial v}{\partial x} = -\frac{Kg}{\nu}\left(\beta\frac{\partial T}{\partial x} + \beta_c\frac{\partial C}{\partial x}\right) \tag{7}$$

where β and β_c are the volumetric thermal and concentration expansion coefficients.

The focus of the present study is on the transient flow, heat transfer and mass transfer phenomena that evolve from the initial condition sketched in Fig. 1

$$u = v = 0 \quad \text{at} \quad 0 \leqslant x \leqslant L, 0 \leqslant y \leqslant H \tag{8}$$

$$T = T_1 \quad \text{and} \quad C = C_1 \quad \text{at} \quad 0 \leqslant x < L/2, 0 \leqslant y \leqslant H \tag{9}$$

$$T = T_0 \quad \text{and} \quad C = C_0 \quad \text{at} \quad L/2 < x \leqslant L, 0 \leqslant y \leqslant H. \tag{10}$$

The conservation equations were solved subject to the following boundary conditions:

$$u = 0, \frac{\partial T}{\partial x} = 0, \frac{\partial C}{\partial x} = 0 \quad \text{at} \quad x = 0, L \tag{11}$$

$$v = 0, \frac{\partial T}{\partial y} = 0, \frac{\partial C}{\partial y} = 0 \quad \text{at} \quad y = 0, H. \tag{12}$$

3. NUMERICAL EXPERIMENTS

The problem formulated in the preceding section was solved in dimensionless form via finite differences. Introducing the dimensionless variables

$$(\hat{x}, \hat{y}) = \frac{(x, y)}{H}, \quad (\hat{u}, \hat{v}) = \frac{(u, v)}{\alpha/H} \tag{13}$$

$$\hat{T} = \frac{T - T_0}{T_1 - T_0}, \quad \hat{C} = \frac{C - C_0}{C_1 - C_0} \tag{14}$$

$$\hat{t} = \frac{t}{\sigma H^2/\alpha} \tag{15}$$

and the dimensionless streamfunction $\hat{\psi} = \psi/\alpha$

$$\hat{u} = \partial\hat{\psi}/\partial\hat{y}, \quad \hat{v} = -\partial\hat{\psi}/\partial\hat{x} \tag{16}$$

the dimensionless form of the conservation equations is

$$\nabla^2\hat{\psi} = -Ra\left(\frac{\partial\hat{T}}{\partial\hat{x}} + N\frac{\partial\hat{C}}{\partial\hat{x}}\right) \tag{17}$$

$$\frac{\partial\hat{T}}{\partial\hat{t}} + \frac{\partial(\hat{T}, \hat{\psi})}{\partial(\hat{x}, \hat{y})} = \nabla^2\hat{T} \tag{18}$$

$$\frac{\phi}{\sigma}\frac{\partial\hat{C}}{\partial\hat{t}} + \frac{\partial(\hat{C}, \hat{\psi})}{\partial(\hat{x}, \hat{y})} = Le^{-1}\nabla^2\hat{C} \tag{19}$$

where $\nabla^2 = \partial^2/\partial\hat{x}^2 + \partial^2/\partial\hat{y}^2$. The dimensionless groups Ra, N and Le appearing in these equations are the Darcy–modified Rayleigh number based on height, the buoyancy ratio and the Lewis number

$$Ra = \frac{Kg\beta H(T_1 - T_0)}{\alpha\nu}, \quad N = \frac{\beta_c(C_1 - C_0)}{\beta(T_1 - T_0)}, \quad Le = \frac{\alpha}{D}. \tag{20}$$

The dimensionless initial and boundary conditions in the streamfunction formulation are

$$\hat{\psi} = 0 \quad \text{at} \quad 0 \leqslant \hat{x} \leqslant L/H, 0 \leqslant \hat{y} \leqslant 1 \tag{21}$$

$$\hat{T} = \hat{C} = 1 \quad \text{at} \quad 0 \leqslant \hat{x} < L/(2H), 0 \leqslant \hat{y} \leqslant 1 \tag{22}$$

$$\hat{T} = \hat{C} = 0 \quad \text{at} \quad L/(2H) < \hat{x} \leqslant L/H, 0 \leqslant \hat{y} \leqslant 1 \tag{23}$$

and

$$\hat{\psi} = 0, \quad \frac{\partial\hat{T}}{\partial\hat{x}} = 0, \quad \frac{\partial\hat{C}}{\partial\hat{x}} = 0 \quad \text{at} \quad \hat{x} = 0, L/H \tag{24}$$

$$\hat{\psi} = 0, \quad \frac{\partial\hat{T}}{\partial\hat{y}} = 0, \quad \frac{\partial\hat{C}}{\partial\hat{y}} = 0 \quad \text{at} \quad \hat{y} = 0, 1. \tag{25}$$

The numerical scheme consisted of approximating all the spatial derivatives at the interior grid points by centered finite differences. The two-step alternating direction implicit method (ADI) was used in order to calculate from equations (18) and (19) the temperature and concentration distributions. The streamfunction was then calculated with equation (17) using the successive overrelaxation method [9]. Each iteration step consisted of (1) separately solving equations (18) and (19) for $\hat{T}$ and $\hat{C}$ using the latest $\hat{\psi}$, and (2) updating the $\hat{\psi}$ field by solving equation (17). Once the temperature and concentration field solutions had converged, the convergence of the flow field $\hat{\psi}$ was guaranteed because equation (17) is linear and the source term depends only on $\hat{T}$ and $\hat{C}$. The numerical values of $\hat{T}$ and $\hat{C}$ on the four boundaries were calculated using the three-node approximation of the gradient normal to the wall. The numerical work of updating the streamfunction field was repeated until the changes in $\hat{\psi}$ at every node became small enough to satisfy the convergence criterion

$$\left|\frac{\hat{\psi}_{new} - \hat{\psi}_{old}}{\hat{\psi}_{new}}\right| < 0.0005. \tag{26}$$

All the numerical solutions reported in this paper were obtained using a uniform grid in which 40 lines covered a length H (e.g. a grid of 40×40 lines in a square domain, $H/L = 1$). Extensive numerical accuracy tests of the type exhibited in Fig. 2 indicated that the fineness of the chosen grid is adequate. Figure 2

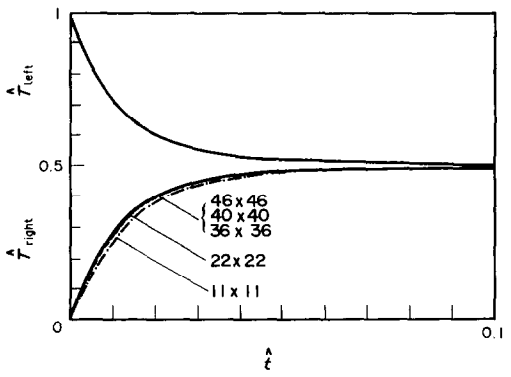

FIG. 2. Numerical accuracy test showing the diminishing effect of grid size: the evolution of the average temperatures of the left and right halves of the porous medium ($N = 0$, $Ra = 100$, $H/L = 1$, $\phi/\sigma = 1$).

shows a typical example of the evolution of the average temperatures computed for the original left and right halves of the rectangular system (the definition of $\hat{T}_{left}$ and $\hat{T}_{right}$ is presented in the next section).

4. THE APPROACH TO THERMAL STRATIFICATION BY CONVECTION

The interplay between the five dimensionless groups that appear in the above problem statement (Ra, Le, N, H/L, ϕ/σ) is responsible for the diversity of flow, heat and mass transfer regimes that rule the eventual approach to thermal and chemical equilibrium. The mission of what follows is to sort out these regimes and to identify in each case the proper time scales of approach to equilibrium. Following the nomenclature developed for natural convection with combined buoyancy effects in porous media (ref. [8], pp. 335–338), we first focus on 'heat-transfer-driven flows' in which the buoyancy effect is due solely to temperature gradients ($N = 0$).

Figure 3 shows a representative sequence of streamline and isotherm patterns in a square domain at one of the highest Rayleigh numbers considered in this study. The flow consists of a single roll the tendency of which is to 'rearrange' the fluid into a position of stable stratification, one in which the warm fluid that initially occupied the left half occupies eventually the upper half of the domain. The 90° turn executed by the mean orientation of the temperature gradient is illustrated by the isotherm patterns. Throughout this rotation the temperature step between the two halves of the fluid inventory is being smoothed away by the effect of thermal diffusion. This effect continues to manifest itself in the vertical direction as the fluid becomes stably stratified, i.e. when the flow dies down and the system tends towards an isothermal state.

The numbers listed in vertical columns to the right of the streamline patterns of Fig. 3 represent the absolute values of $\hat{\psi}$ corresponding to each streamline, such that the largest value belongs to the innermost streamline (the actual $\hat{\psi}$ values are negative). The numbers listed next to each isotherm pattern denote the respective $\hat{T}$ values of the isotherms. The $\hat{T}$ values decrease from left to right or from top to bottom through each bundle of isotherms. The same meaning is attached to the $\hat{\psi}$ values listed in Figs. 4, 5 and 10.

In the very beginning of this phenomenon (e.g. $\hat{t} = 10^{-6}$ in Fig. 3) the flow and temperature fields are nearly symmetric with respect to the vertical midplane of the system. The time scales of the approach to thermal equilibrium can be determined on the basis of scale analysis. The $\hat{t} = 0^+$ condition is one characterized by a pressure imbalance between the right and left halves of the system of Fig. 1. The warm fluid that occupies the left side has a vertical hydrostatic pressure gradient that is less pronounced than the corresponding gradient on the right (cold) side. The mismatch between the two dP/dy scales gives birth to finite pressure gradients in the horizontal direction. Along the top boundary the finite pressure difference points to the right, and its scale is

$$\Delta P \sim g(\rho_{left} - \rho_{right})H \sim \rho g H \beta \Delta T \qquad (27)$$

where $\Delta T = T_1 - T_0$. The same pressure difference forms along the bottom boundary and tends to push fluid towards the left side of the system. What forms is a horizontal counterflow in which the warm branch flows from left to right along the top.

One effect of this counterflow is that it tilts the imaginary demarcation line between the warm region and the cold region. This tilting effect is made visible by the early shift exhibited by the isotherms, especially in the case of relatively shallow porous domains, $L > H$ (Figs. 4 and 5). If l is the length scale of the segment obtained by projecting the demarcation line on the horizontal direction, then l increases as the time increases (note that in the very beginning $l = 0$, because the demarcation line coincides with the vertical midplane). The length scale l represents also the horizontal distance over which the flow experiences the pressure drop ΔP. The horizontal velocity scale of this flow follows from equation (2)

$$u_1 \sim \frac{K}{\mu}\frac{\Delta P}{l}. \qquad (28)$$

A companion result is the vertical velocity scale of the vertical counterflow that completes the single roll

$$v_1 \sim \frac{u_1 H}{l} \sim \frac{HK\Delta P}{\mu l^2}. \qquad (29)$$

This estimate follows from the argument that the mass flow rate is conserved around a roll of height H and length l, equation (1).

The unknown horizontal length scale l can be determined based on an energy conservation argument centered around equation (4). In the flow region $l \times H$ the scales of the five terms of equation (4) are, in order

$$\sigma\frac{\Delta T}{t}, \quad u_1\frac{\Delta T}{l}, \quad v_1\frac{\Delta T}{H}, \quad \alpha\frac{\Delta T}{l^2}, \quad \alpha\frac{\Delta T}{H^2}. \qquad (30)$$

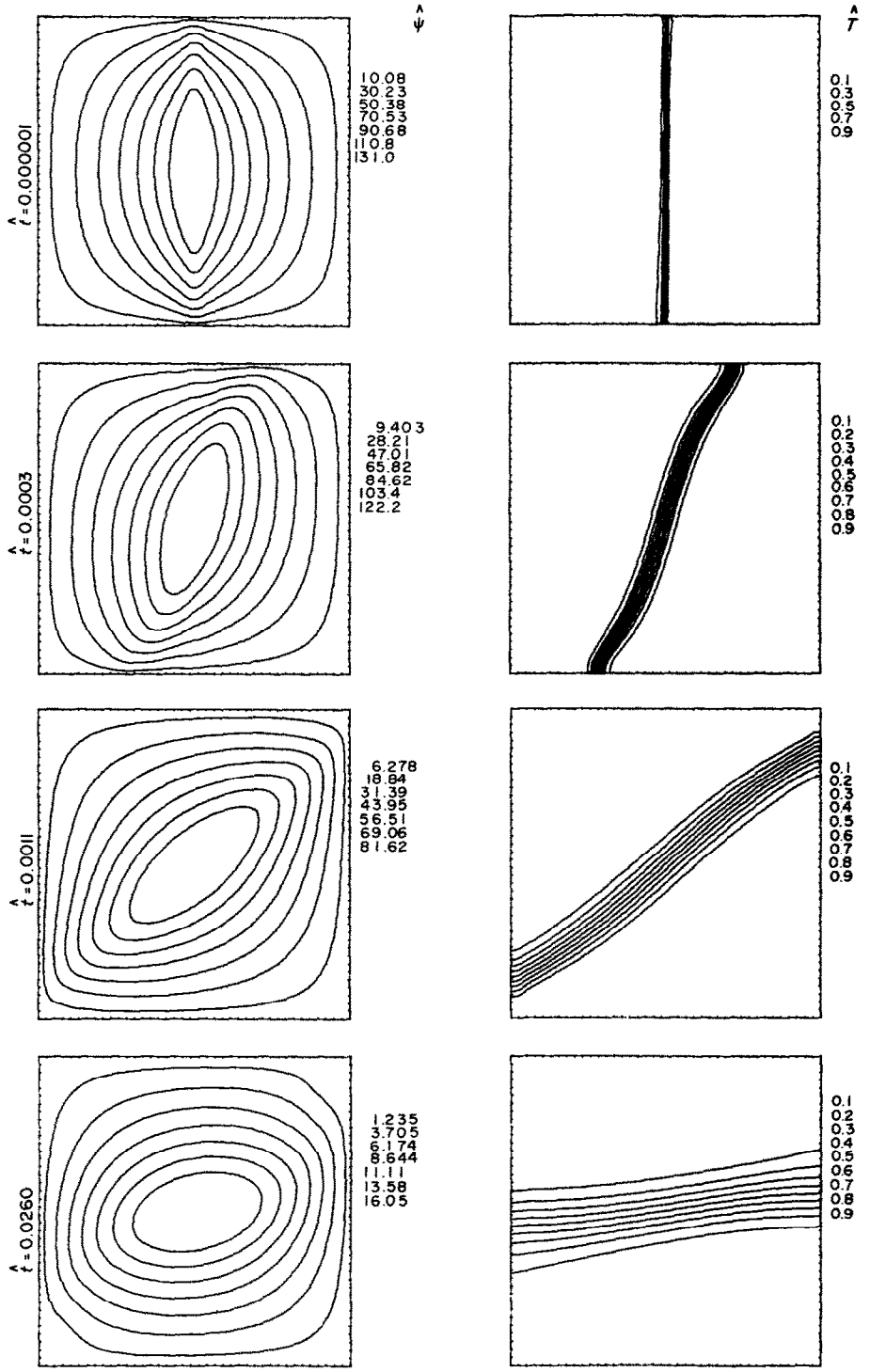

FIG. 3. The streamline and temperature fields vs time in a heat-transfer-driven flow ($N = 0$, $Ra = 10^3$, $H/L = 1$, $\phi/\sigma = 1$). Note that the constant $\hat{T}$ lines are the same as the constant $\hat{C}$ lines when $Le = 1$.

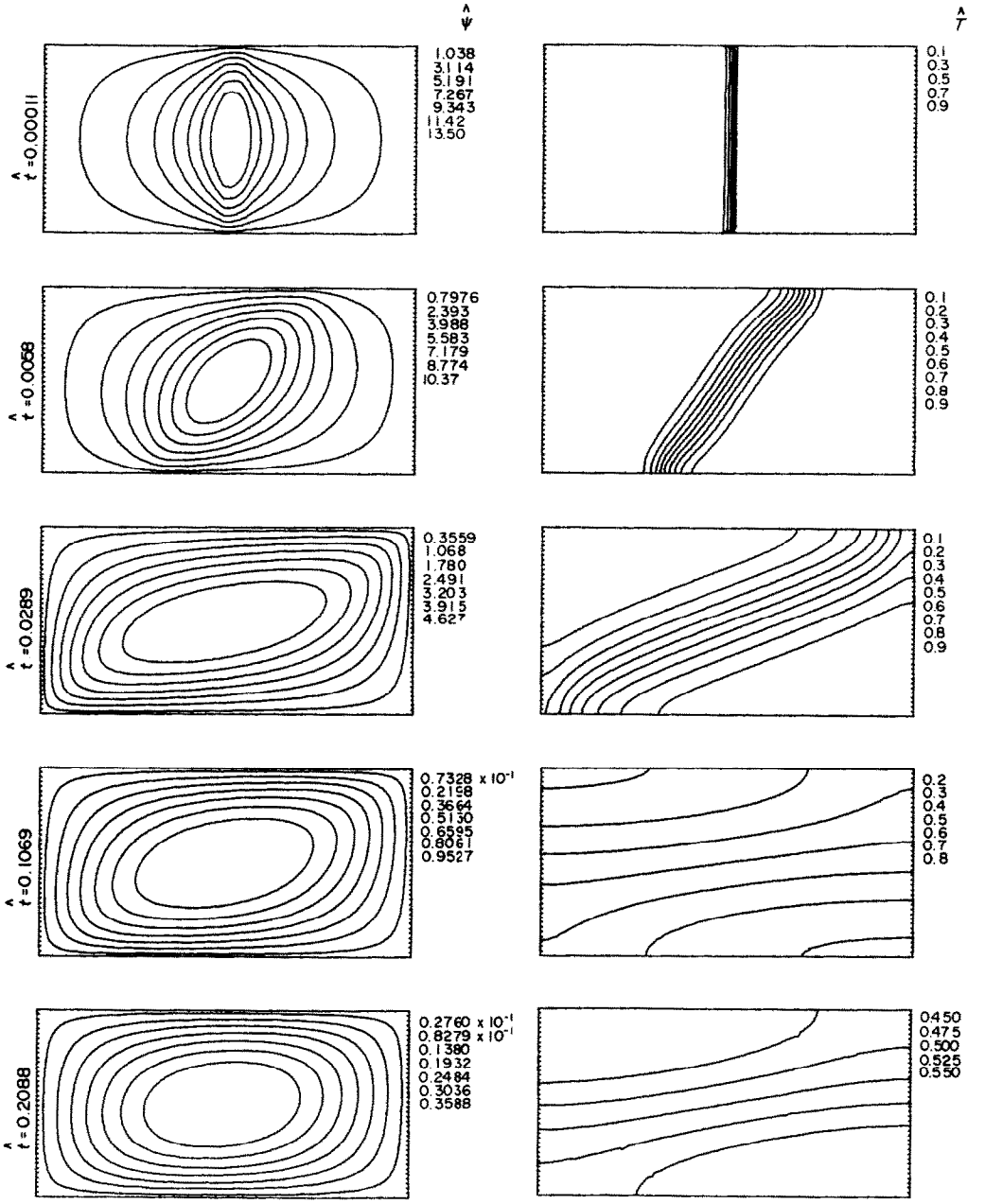

FIG. 4. The evolution of the heat-transfer-driven flow in a $H/L = 0.49$ shallow porous medium ($N = 0$, $Ra = 100$, $\phi/\sigma = 1$).

In view of the mass conservation scaling (29), namely $u_1/l \sim v_1/H$, we note that the second and third scales listed above (the 'convection' scales) are equal. This observation becomes more visible after dividing the five scales by the horizontal thermal diffusion scale $\alpha\Delta T/l^2$: using equations (28) and (29) we obtain in order

$$\frac{\sigma l^2}{\alpha t}, Ra, Ra, 1, \left(\frac{l}{H}\right)^2 \tag{31}$$

where Ra is the Darcy–modified Rayleigh number defined in equation (20). It is clear that in the high Rayleigh number regime considered in this study, the energy balance can only be between the convection scale (Ra) and the thermal inertia scale ($\sigma l^2/\alpha t$), which means

$$l \sim \left(\frac{\alpha t}{\sigma} Ra\right)^{1/2} \tag{32}$$

and, via equations (28) and (29)

$$u_1 \sim \left(\frac{\sigma\alpha}{t} Ra\right)^{1/2} \tag{33}$$

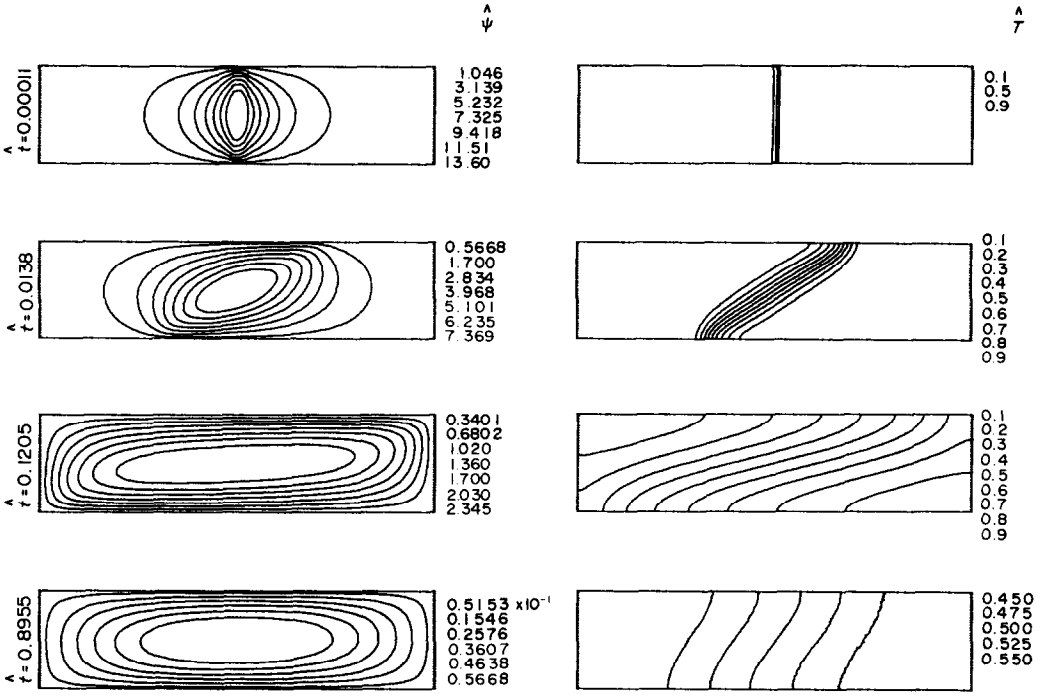

FIG. 5. The evolution of the heat-transfer-driven flow in a $H/L = 0.25$ shallow porous medium ($N = 0$, $Ra = 100$, $\phi/\sigma = 1$).

$$v_1 \sim \frac{\sigma H}{t}. \tag{34}$$

The streamfunction scale is $\psi \sim uH$, or in dimensionless terms

$$\hat{\psi} \sim Ra^{1/2} \hat{t}^{-1/2}. \tag{35}$$

In order for equations (32)–(35) to be valid, the thermal diffusion scales listed in (31) must be negligible relative to convection and thermal inertia, in other words

$$Ra > \left(\frac{l}{H}\right)^2 \tag{36}$$

or, after using equation (32) and equation (15)

$$\hat{t} < 1. \tag{36'}$$

The convection dominated flow described until now continues until the imaginary demarcation line and the isotherms become horizontal, If $L > H$, the temperature field becomes 'stratified' by convection when l has had time to become of order L. In view of equation (32), that time is

$$\hat{t}_1 \sim \left(\frac{L}{H}\right)^2 Ra^{-1}. \tag{37}$$

Assuming that the $\hat{t}_1$ scale estimated above is less than one, i.e. that criterion (36′) holds, the process of horizontal layering (stratification) by convection is followed by a regime of pure thermal diffusion in the vertical direction. The ultimate effect of this process is to smooth away the vertical temperature gradient that existed at $\hat{t} \sim \hat{t}_1$. The time scale of the vertical thermal diffusion regime is $t \sim \sigma H^2/\alpha$, hence the dimensionless time for the establishment of the isothermal state

$$\hat{t}_2 \sim 1. \tag{38}$$

The assumption that the $\hat{t}_1$ scale (37) is less than one means that the temperature field becomes stratified by convection ($l \sim L$) *before* vertical thermal diffusion has time to act. This assumption holds at high *Ra's* and moderate L/H ratios, as in the numerical experiments conducted in this study. The $\hat{t}_1 < 1$ assumption breaks down in the shallow porous medium limit $L/H \to \infty$, which for steady-state convection was treated in refs. [10, 11]. We focus on the $L/H \to \infty$ limit in Section 6.

5. COMPARISON WITH NUMERICAL EXPERIMENTS

The trends and orders of magnitude predicted theoretically in Section 4 are validated by numerical experiments. A crucial result is the time scale $\hat{t}_1$, which marks the end of the process of stratification by convection, that is, the end of the *horizontal* heat transfer interaction between the original left and right halves of the system. In order to verify the correctness of the $\hat{t}_1$ scale (37) we first designed a method to

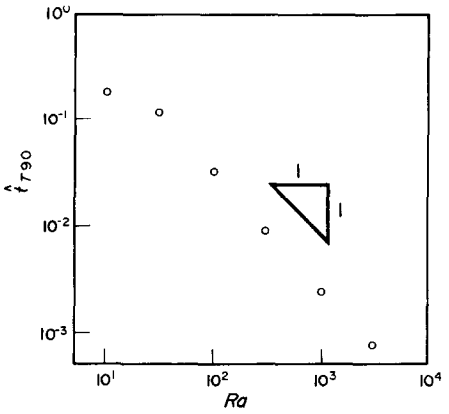

FIG. 6. The Ra dependence of the time marking the end of horizontal convective heat transfer ($N = 0$, $H/L = 1$, $\phi/\sigma = 1$).

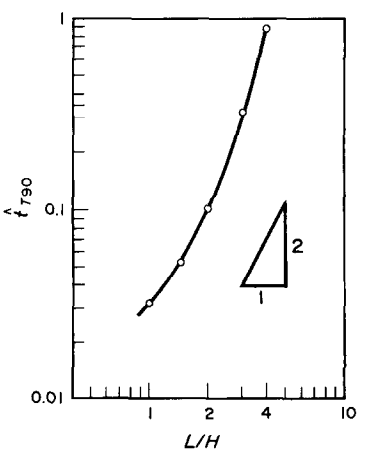

FIG. 7. The H/L dependence of the time marking the end of horizontal convective heat transfer ($N = 0$, $Ra = 100$, $\phi/\sigma = 1$).

estimate the 'end' of heat transfer through the vertical midplane $x = L/2$. We first calculated the average temperatures of the original left and right halves of the domain

$$\hat{T}_{\text{left}}(\hat{t}) = 2\frac{H}{L}\int_{\hat{x}=0}^{L/2H}\int_{\hat{y}=0}^{1}\hat{T}(\hat{x},\hat{y},\hat{t})\,d\hat{x}\,d\hat{y} \quad (39)$$

$$\hat{T}_{\text{right}}(\hat{t}) = 2\frac{H}{L}\int_{\hat{x}=L/2H}^{L/H}\int_{\hat{y}=0}^{1}\hat{T}(\hat{x},\hat{y},\hat{t})\,d\hat{x}\,d\hat{y} \quad (40)$$

and studied their behavior as $\hat{t}$ increases. Figure 2 shows the symmetry of the approach to the final average temperature of 1/2: this approach occurs within a characteristic time interval. Note also that the slope of each curve is proportional to the respective heat transfer interaction through the vertical midplane. For the sake of concreteness we defined the left-to-right heat exchange as being practically 'complete' when

$$\hat{T}_{\text{left}} = 0.55 \quad \text{or} \quad \hat{T}_{\text{right}} = 0.45 \quad (41)$$

that is, when 90% of the total heat exchange has already taken place. The dimensionless time when the numerical solution met conditions (41) was labeled $\hat{t}_{T90}$.

Figure 6 shows that the calculated $\hat{t}_{T90}$ values decrease linearly with Ra, in accordance with the theoretical scaling law (37). This trend is particularly visible in the high Rayleigh number limit, which is a basic assumption in the foundation of the scale analysis (see equations (36) and (31)). Furthermore, the calculated $\hat{t}_{T90}$ values are consistently of the same order as the $\hat{t}_1$ values provided by equation (37).

The correctness of the $\hat{t}_1$ scale (37) is tested further in Fig. 7, which shows that at constant Ra the $\hat{t}_{T90}$ scale increases as the horizontal extent of the medium increases. The theoretical trend (37) is indicated by a short segment of slope 2 : 1. The calculated $\hat{t}_{T90}$ values confirm this trend only if the order of magnitude of $\hat{t}_{T90}$ is less than one, i.e. when criterion (36′) is satisfied. In the shallow enclosure limit criterion (36′) fails and the calculated $\hat{t}_{T90}$ values are substantially larger than those calculated based on equation (37).

The overall behavior of the flow field can be tested through the streamfunction scaling law (35). As a measure of the order of magnitude of $\hat{\psi}$ we took the streamfunction maximum $\hat{\psi}_{\max}$, which is always located in the geometric center of the rectangular domain. Figure 8 shows that the theoretical scaling law (35) can be used successfully to correlate the $\hat{\psi}_{\max}$ values revealed by numerical experiments. Plotted on the ordinate is $\hat{\psi}_{\max}$ divided by $Ra^{1/2}$: this group decreases as $\hat{t}^{-1/2}$ provided $\hat{t}$ is small enough so that the flow does not reach the left and right extremities of the rectangular domain. In other words, as was noted earlier, scaling law (35) is valid if $\hat{t} < \hat{t}_1$, where $\hat{t}_1$ is given by equation (37).

The numerical experiments that here are sampled through Figs. 3–5 show more than the purely 'convective' features that were addressed in the scale analysis of Section 4. Superimposed on the high Rayleigh number flow is the effect of thermal diffusion that begins at $\hat{t} = 0^+$ and tends to erase the demarcation line between the warm and cold sections of the porous medium. This effect induces its own 'secondary' flow which is associated with the thermal boundary layers that grow on both sides of the originally vertical

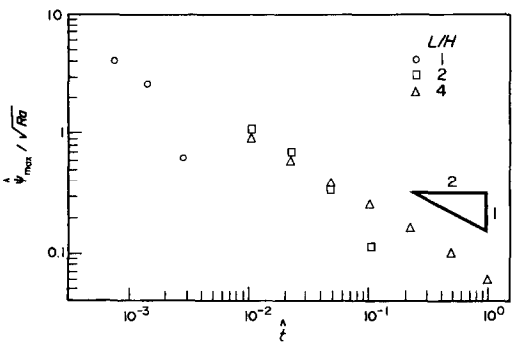

FIG. 8. Correlating the calculated short-time $\hat{\psi}_{\max}$ values using the streamfunction scaling law (35).

demarcation line. The horizontal length scale (thickness) of this flow, δ, is dictated originally by a balance between horizontal diffusion and thermal inertia, hence

$$\delta \sim \left(\frac{\alpha t}{\sigma}\right)^{1/2}. \tag{42}$$

Equation (32) shows that this thermal diffusion thickness is always negligible when compared with l

$$\frac{\delta}{l} \sim Ra^{-1/2} < 1. \tag{43}$$

Following an argument identical to the one used by Poulikakos and Bejan [12] in the study of transient boundary layer convection in a confined porous medium heated from the side (see also ref. [8], pp. 388–394), one can show that δ reaches a terminal (final) value at a time of order

$$\hat{t}_0 \sim Ra^{-1}. \tag{44}$$

Beyond this time the δ_0-thin diffusion stripe along the demarcation line is ruled by a balance between horizontal diffusion and vertical convection

$$\delta_0 \sim \left(\frac{\alpha t_0}{\sigma}\right)^{1/2} \sim H Ra^{1/2}. \tag{45}$$

The velocity scales in the $\delta_0 \times H$ region are

$$u_0 \sim \frac{\alpha}{H} Ra^{1/2} \tag{46}$$

$$v_0 \sim \frac{\alpha}{H} Ra. \tag{47}$$

The presence of this secondary flow is most visible in the isotherm patterns of Figs. 3–5, not in the slender vertical stripe of thickness δ_0 and height H, but in the incipient horizontal 'intrusions' that form along the top and bottom boundaries. For example, the second $\hat{T}$-frame of Fig. 3 shows that the tilting demarcation line is shaped more like the integral sign '$\int$', and that the upper extremity of this shape is associated with a horizontal intrusion layer the movement to the right of which accentuates (is added to) the displacement l that was discussed in Section 4. The scales of these horizontal intrusion layers can be determined by following the v_0 vertical flow as it hits the top boundary and turns the corner [12]. They are not repeated here because the secondary flow has a negligible effect relative to the instantaneous heat transfer rate between the two thermally distinct regions of the porous medium.

This last assertion can be expressed analytically by estimating the ratio between the horizontal heat transfer rate associated with the convective counterflow of Section 4

$$q_1 \sim (\rho c_p)_f u_1 H \Delta T \sim k \Delta T Ra^{1/2} \hat{t}^{-1/2} \tag{48}$$

and the corresponding quantity associated with the diffusion-driven secondary flow

$$q_0 \sim k \Delta T Ra^{1/2}. \tag{49}$$

That ratio turns out to be

$$\frac{q_1}{q_0} \sim \hat{t}^{-1/2} \tag{50}$$

which, in view of the time criterion (37) and the assumption listed immediately after it, is a number the order of magnitude of which is greater than one.

6. THE SHALLOW LAYER LIMIT

The scenario painted in the preceding discussion and Figs. 3–5 refers to high Ra flows in layers the slenderness ratio L/H of which is sufficiently moderate so that the $\hat{t}_1$ scale (37) is smaller than one. Physically, $\hat{t}_1 < 1$ means that the layer achieves a state of stable stratification as a result of convection before the stratification can be smoothed away by vertical thermal diffusion over the height H. The $\hat{t}_1 < 1$ condition becomes threatened as the ratio L/H increases. Note, for example, the last two isotherm patterns exhibited in Fig. 5, for which the $\hat{t}_1$ value calculated with equation (37) is 0.16—a number the order of magnitude of which is not much different than one. The slope of the isotherms decreases through the first three patterns of isotherms, however, this trend is reversed in the last frame where the effect of vertical thermal diffusion is to rearrange the temperature field so that it depends mainly on longitudinal position and time.

The features that begin to become visible in the last isotherm pattern of Fig. 5 are preserved by a very simple analytical solution that holds strictly in the limit $L/H \to \infty$. The method of solution is identical to the one employed in a related problem [10, 11], therefore, we list only the problem statement and the key results. We begin with a different set of dimensionless variables based on the correct scales of the slender layer limit, namely

$$\tilde{x} = \frac{x}{L}, \quad \tilde{t} = \frac{t}{\sigma L^2/\alpha}, \quad \tilde{\psi} = \psi \frac{vL}{Kg\beta H^2 (T_1 - T_0)} \tag{51}$$

and the $\hat{y}$ and $\hat{T}$ variables defined already in equations (13) and (14). The momentum equation for heat-transfer-driven flow and the energy equation are

$$\varepsilon \frac{\partial^2 \tilde{\psi}}{\partial \tilde{x}^2} + \frac{\partial^2 \tilde{\psi}}{\partial \hat{y}^2} = -\frac{\partial \hat{T}}{\partial \tilde{x}} \tag{52}$$

$$\varepsilon \frac{\partial \hat{T}}{\partial \tilde{t}} + \varepsilon Ra \left(\frac{\partial \tilde{\psi}}{\partial \hat{y}} \frac{\partial \hat{T}}{\partial \tilde{x}} - \frac{\partial \tilde{\psi}}{\partial \tilde{x}} \frac{\partial \hat{T}}{\partial \hat{y}} \right) = \varepsilon \frac{\partial^2 \hat{T}}{\partial \tilde{x}^2} + \frac{\partial^2 \hat{T}}{\partial \hat{y}^2} \tag{53}$$

where ε is the small parameter $\varepsilon = (H/L)^2$. For the series solution

$$(\tilde{\psi}, \hat{T}) = (\tilde{\psi}, \hat{T})_0 + \varepsilon (\tilde{\psi}, \hat{T})_1 + \varepsilon^2 (\tilde{\psi}, \hat{T})_2 + \ldots \tag{54}$$

and for the boundary conditions of Fig. 1, we obtain in order

$$\hat{T}_0 = f_0(\tilde{x}, \tilde{t}), \quad \text{unknown} \tag{55}$$

$$\tilde{\psi}_0 = \left(\frac{1}{8} - \frac{1}{2}\hat{y}^2\right)\frac{\partial f_0}{\partial \tilde{x}} \quad (56)$$

$$\hat{T}_1 = Ra\left(\frac{1}{8}\hat{y} - \frac{1}{6}\hat{y}^3\right)\left(\frac{\partial f_0}{\partial \tilde{x}}\right)^2 + f_1(\tilde{x}, \tilde{t}). \quad (57)$$

The series solution is similar to the one known for the steady-state problem, in which the functions f_0, f_1, etc. are linear functions of x only. In the present problem, an additional conclusion that is reached in the derivation of the $\hat{T}_1$ expression (57) is that f_0 must satisfy the equation

$$\frac{\partial f_0}{\partial \tilde{t}} = \frac{\partial^2 f_0}{\partial \tilde{x}^2}. \quad (58)$$

This conclusion follows from invoking the adiabatic top and bottom boundary conditions in the development of equation (57). The solution to equation (58) is obviously the solution for transient one-dimensional heat conduction in a finite medium with insulated extremities and 'step' initial temperature distribution

$$f_0(\tilde{x}, \tilde{t}) = \frac{1}{2} - \frac{2}{\pi}\sum_{n=0}^{\infty}(2n+1)^{-1} \times \sin\left[(2n+1)\pi\left(\tilde{x} - \frac{1}{2}\right)\right] \times \exp\left[-(2n+1)^2\pi^2\tilde{t}\right]. \quad (59)$$

Therefore, regardless of the size of Ra (finite) and the presence of longitudinal counterflow, in the $L/H \to \infty$ limit the temperature field is the same as for transient longitudinal thermal diffusion. The isotherms are vertical, equations (55) and (59). In the beginning the the temperature drop is concentrated near the midplane ($\tilde{x} = 1/2$), and so is the flow, equation (56). The longitudinal extent of the temperature drop and flow field increases like $(\alpha t/\sigma)^{1/2}$ as long as $(\alpha t/\sigma)^{1/2}$ is smaller than L.

The only numerical experiments that in this study begin to illustrate the features of convection in the shallow-layer limit are those presented for $H/L = 0.25$ in Fig. 5. The theoretical result developed in this section deserves to be tested through a special series of numerical experiments that focus especially on the shallow layer geometry. The cost associated with running small H/L cases based on the numerical scheme described in Section 3 did not allow us to study shallow geometries with H/L values less than 1/4.

7. APPROACH TO UNIFORM CONCENTRATION VIA HEAT-TRANSFER-DRIVEN NATURAL CONVECTION

We now turn our attention to the mass transfer phenomenon that rides on the heat-transfer-driven flow discussed until now, $|N| \ll 1$. The important questions are 'at what time is the medium practically in a state of vertical concentration stratification, or in a state of uniform concentration?', and 'what parameters govern these time scales, and how ?'

In a scale analysis that is patterned after equations (30)–(37), we focus on the earliest stages of the flow (u_1, v_1, known) and consider the tilting of the imaginary interface that originally separated the $C = C_1$ domain from the $C = C_0$ domain. Let l_C be the length scale of the projection of this interface on the horizontal direction. In the central region of length l_C and height H, at sufficiently high Rayleigh numbers we expect a balance between convection and inertia, in this case, between mass convection and mass inertia. Guided by the first two terms of equaion (5) we express this balance as

$$\phi\frac{\Delta C}{t} \sim u_1\frac{\Delta C}{l_C} \quad (60)$$

which, using equation (33), yields

$$l_C \sim \frac{\sigma}{\phi}\left(\frac{\alpha t}{\sigma}Ra\right)^{1/2} \sim \frac{\sigma}{\phi}l. \quad (61)$$

Therefore, in general, the position of the tilting concentration interface differs from that of the temperature interface, in the way that σ differs from ϕ. When l_C grows to be of order L, the concentration field becomes stratified by convection (i.e. the constant C lines become practically horizontal). Let t_3 be the time scale when $l_C \sim L$; from equation (61) we deduce that

$$\hat{t}_3 \sim \left(\frac{\phi}{\sigma}\right)^2\left(\frac{L}{H}\right)^2 Ra^{-1}. \quad (62)$$

At times greater than t_3 the smoothing of the concentration field is done by pure mass diffusion in the vertical direction. The time scale (t_4) of this final step towards a state of uniform concentration is obtained by writing

$$\phi\frac{\Delta C}{t_4} \sim D\frac{\Delta C}{H^2} \quad (63)$$

which in dimensionless form yields

$$\hat{t}_4 \sim \frac{\phi}{\sigma}Le. \quad (64)$$

The scenario described until now holds if $\hat{t}_3 < \hat{t}_4$, in other words if

$$Le\,Ra > \frac{\phi}{\sigma}\left(\frac{L}{H}\right)^2. \quad (65)$$

Or, we may reason that the above scenario holds if the assumed convection–inertia balance is correct, i.e. if vertical mass diffusion is negligible when compared (at a time of order t_3) with horizontal convection

$$D\frac{\Delta C}{H^2} < u_1\frac{\Delta C}{l_C}. \quad (66)$$

It is easy to show that the restriction imposed by equation (66) is exactly the same as equation (65).

When criterion (65) is not satisfied, the con-

centration field evolves as a set of nearly vertical constant C lines (the effect of vertical mass diffusion is pronounced). This phenomenon is analogous to the shallow-layer thermal convection limit presented in Section 6. Despite the presence of a counterflow, the final state of uniform concentration is achieved via pure mass diffusion in the horizontal direction. If t_5 is the time scale of this process, then the inertia–diffusion balance

$$\phi\frac{\Delta C}{t_5}\sim D\frac{\Delta C}{L^2} \tag{67}$$

yields

$$t_5\sim\frac{\phi}{\sigma}\left(\frac{L}{H}\right)^2 Le. \tag{68}$$

One way to test the validity of these scaling predictions is to estimate the effective time when the net mass transfer through the vertical midplane ceases. The corresponding theoretical scales are t_3 for the convection regime, and t_5 for the diffusion regime. In the course of one numerical experiment we can keep track of the gross movement of the species the concentration of which is C, by calculating the average concentrations on the left and right sides of the vertical midplane

$$\hat{C}_{\text{left}}(\hat{t})=2\frac{H}{L}\int_{\hat{x}=0}^{L/2H}\int_{\hat{y}=0}^{1}\hat{C}(\hat{x},\hat{y},\hat{t})\,\mathrm{d}\hat{x}\,\mathrm{d}\hat{y} \tag{69}$$

$$\hat{C}_{\text{right}}(\hat{t})=2\frac{H}{L}\int_{\hat{x}=L/2H}^{H/L}\int_{\hat{y}=0}^{1}\hat{C}(\hat{x},\hat{y},\hat{t})\,\mathrm{d}\hat{x}\,\mathrm{d}\hat{y}. \tag{70}$$

The quantities behave the same way as the average temperatures exhibited in Fig. 2, namely, $\hat{C}_{\text{left}}(0)=1$, $\hat{C}_{\text{right}}(0)=0$ and $\hat{C}_{\text{left}}(\infty)=\hat{C}_{\text{right}}(\infty)=1/2$. Let $\hat{t}_{C90}$ represent the time when 90% of the total left → right mass exchange has taken place, i.e. the time when

$$\hat{C}_{\text{left}}=0.55\quad\text{and}\quad\hat{C}_{\text{right}}=0.45. \tag{71}$$

Figure 9 shows the dependence of $\hat{t}_{C90}$ on the Lewis number, in an experiment in which Ra is high and fixed. At small Lewis numbers, when the mass diffusivity D greatly exceeds the thermal diffusivity α, the horizontal mass transfer is by diffusion and its time scale is t_5. Note that $\hat{t}_{C90}$ increases linearly as Le increases, which confirms the theoretical result (68). At high Lewis numbers $\hat{t}_{C90}$ is independent of Le, as

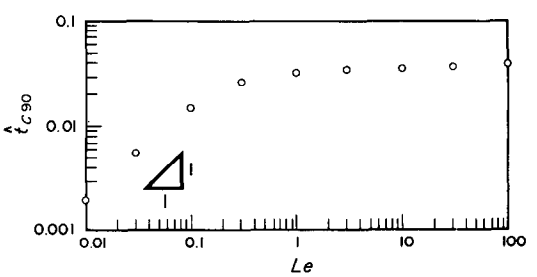

FIG. 9. The Le dependence of the time marking the end of net horizontal mass transfer ($Ra=100$, $H/L=1$, $\phi/\sigma=1$).

anticipated in equation (62). In this range the left → right mass transfer is by convection, leading first to a state of mass stratification (horizontal constant C lines) followed by pure mass diffusion in the vertical direction.

The transition from a regime of horizontal mass convection to one of horizontal diffusion is illustrated in Fig. 10, in an experiment where Le decreases at constant Ra. In fact, the start of this sequence of experimental results is the set of constant $\hat{T}$ lines of Fig. 3, which are identical to the constant $\hat{C}$ lines representing the case $Le=1$. Therefore, taken together, Figs. 3 and 10 show what happens as Le assumes successively the values 1, 0.1 and 0.01. The flow that is responsible for these patterns does not change from one time sequence to the next (this heat-transfer-driven flow is shown in Fig. 3). It is clear that as Le decreases the sharpness of the C_1/C_0 dividing line disappears, as the phenomenon of mass diffusion takes over.

8. MASS-TRANSFER-DRIVEN FLOWS

The heat and mass transfer processes discussed until now were all tied to a flow driven by the buoyancy effect due to temperature gradients ($|N|\ll 1$). The processes that occur in the opposite extreme (mass-driven flows, $|N|\gg 1$) can be studied and sorted out in an entirely analogous manner. This, we have done; in the interest of conciseness, however, we list the main scales that differentiate between the various mass-transfer-driven regimes. The analysis consists of redoing all the work that started with equation (27), this time recognizing the coupling between the flow field (driven) and the concentration field (driving).

The initial counterflow that begins to tilt the concentration interface C_1/C_0 is driven by a longitudinal pressure difference of order $(\Delta P)_m\sim\rho g H\beta_c\Delta C$. Let l_m be the length scale of the projection of the C_1/C_0 interface on the horizontal direction. The scales of the horizontal and vertical velocity components of the initial counterflow are then $K(\Delta P)_m/(\mu l_m)$ and $KH(\Delta P)_m/(\mu l^2)$, respectively.

Considering first the 'convection' regime, in which the C field is turned over and stratified by convection, the balance between mass inertia and mass convection in equation (5) suggests

$$l_m\sim\left(\frac{tD}{\phi}Ra_m\right)^{1/2} \tag{72}$$

where Ra_m is the Darcy–modified Rayleigh number for mass-transfer-driven flow

$$Ra_m=\frac{KgH\beta_c\Delta C}{\nu D}=Ra\,Le\,N. \tag{73}$$

The flow rate (maximum streamfunction) of the counterflow is of order $[\phi Ra_m/(\sigma\hat{t}\,Le)]^{1/2}$. The concentration field becomes stratified by convection when $l_m\sim L$, which corresponds to the time

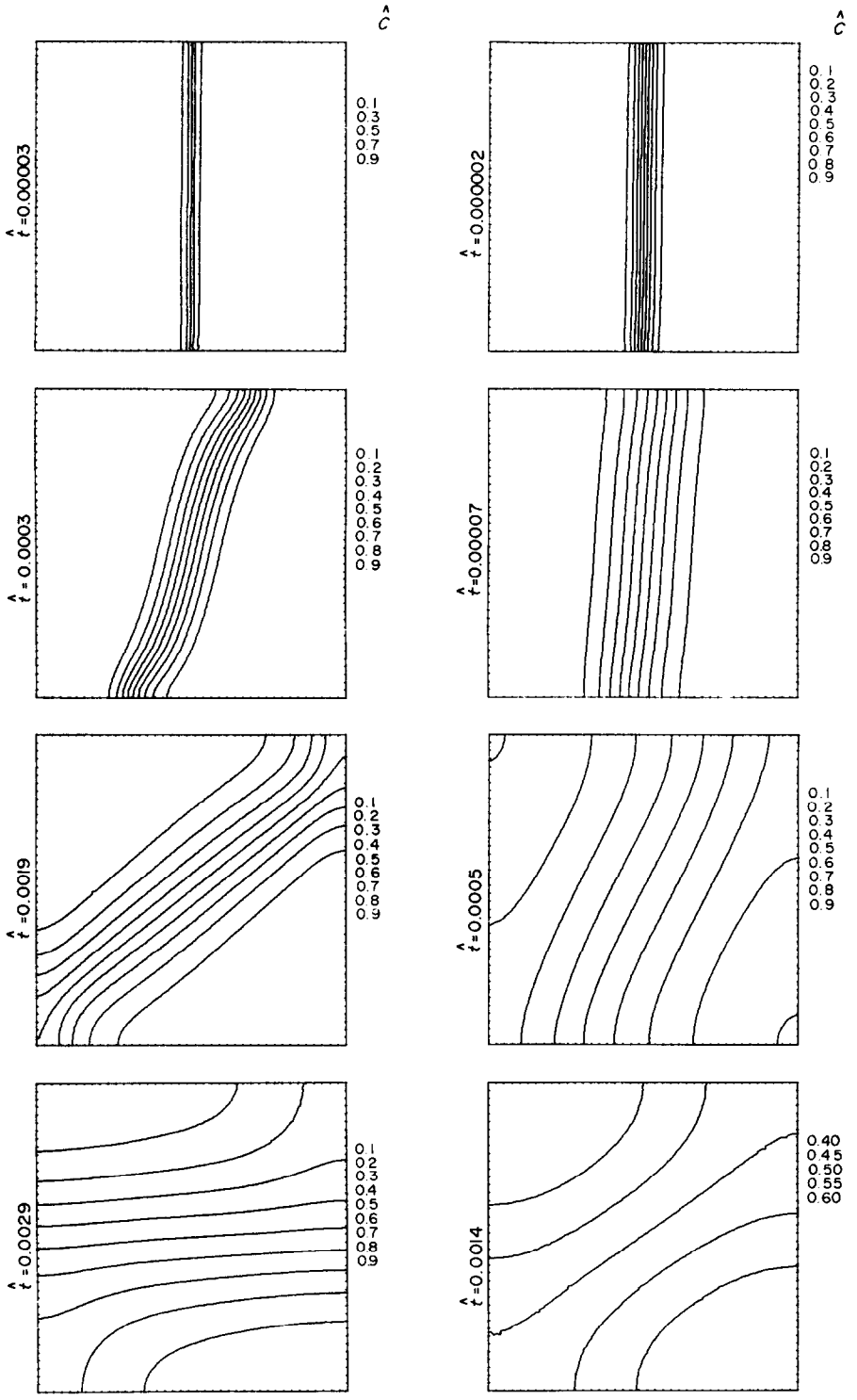

FIG. 10. The effect of Lewis number on the concentration field riding on a heat-transfer-driven flow ($Ra = 10^3$, $H/L = 1$, $\phi/\sigma = 1$): left sequence, $Le = 0.1$; right sequence, $Le = 0.01$.

$$\hat{t}_{1,m} \sim \left(\frac{L}{H}\right)^2 Ra_m^{-1}\, Le \frac{\phi}{\sigma}. \tag{74}$$

Note that this time scale plays the same role in mass-transfer-driven flows as the $\hat{t}_1$ scale of heat-transfer-driven flows, equation (37). Going back to the inertia–convection balance that was assumed in connection with equation (5), the above scales are valid if the effect of diffusion is negligible relative to convection. This condition translates into

$$\hat{t} < \frac{\phi}{\sigma} Le. \tag{75}$$

At times greater than $t_{1,m}$, the stratification of the concentration field is smoothed away by the effect of vertical mass diffusion, the time scale of which is $\phi H^2/D$. In dimensionless terms, the time of the establishment of uniform concentration is

$$\hat{t}_{2,m} \sim \frac{\phi}{\sigma} Le. \tag{76}$$

The fact that $t_{1,m}$ must occur before $t_{2,m}$ means that the assumed mass-transfer-driven flow must be a high Rayleigh number flow, $Ra_m > (L/H)^2$.

The analytical solution developed for the shallow layer limit (Section 6) can be derived also for mass-transfer-driven flows. The important conclusion that follows from this extension is that the time needed for the establishment of a state of uniform concentration is the same as the time of longitudinal mass diffusion over the distance L, namely, the $\hat{t}_5$ scale listed in equation (68). This conclusion holds for any finite Ra_m and Le, strictly in the limit $L/H \to \infty$.

If in the very beginning there is also a temperature difference ΔT between the 'left' and 'right' halves of the porous medium, then the mass-transfer-driven flow described above may affect the approach to thermal equilibrium. Consider first the case when α is sufficiently smaller than D, so that the initial heat transport through the vertical midplane is dominated by convection. Let l_T represent the horizontal deformation (tilting) of the T_1/T_0 interface. Claiming a balance between thermal inertia and thermal convection in the $l_T \times H$ region, when the mass-transfer-driven flow is in the convection regime, yields

$$l_T \sim H\left(\frac{\phi \hat{t}\, Ra_m}{\sigma\, Le}\right)^{1/2} \sim \frac{\phi}{\sigma} l_m. \tag{77}$$

Repeating step-by-step the analysis of Section 7, we find that a state of thermal stratification is achieved by convection when $l_T \sim L$, which means at a time of order

$$t_{3,m} \sim \frac{\sigma}{\phi}\left(\frac{L}{H}\right)^2 \frac{Le}{Ra_m}. \tag{78}$$

At times greater than $t_{3,m}$ the heat transfer process is dominated by vertical thermal diffusion. The temperature field becomes uniform at a time $t_{4,m} \sim \sigma H^2/\alpha$, or $\hat{t}_{4,m} \sim 1$. Note further that part of this scenario is the assumption $\hat{t}_{3,m} < \hat{t}_{4,m}$ which translates into a 'small Lewis number' requirement

$$Le < \frac{\phi}{\sigma}\left(\frac{H}{L}\right)^2 Ra_m. \tag{79}$$

At sufficiently high Lewis numbers the effect of horizontal thermal diffusion dominates. The balance between thermal inertia and longitudinal diffusion suggests that thermal equilibrium is achieved at $t_{5,m} \sim \sigma L^2/\alpha$, which in dimensionless terms means $\hat{t}_{5,m} \sim (L/H)^2$.

9. CONCLUDING REMARKS

Looking back at the ground covered in this study, we see an emphasis on high-Rayleigh-number flows in which convection plays the dominant role. This emphasis may appear to contradict the small temperature difference assumption on which the Boussinesq approximation of the right-hand side of equation (17) is based. We note here that the study of high Rayleigh numbers and the formulation of equation (17) are not incompatible—after all, the bulk of what has been accomplished in the field of natural convection in porous media exhibits the same two features. According to equation $(20)_1$, even if $\beta(T_1 - T_0)$ is much smaller than one, we can think of a sufficiently tall system (H) and/or a sufficiently permeable porous matrix (K) such that Ra is considerably greater than the threshold value required by a convection-dominated regime.

Another interesting observation is that the horizontal flow described in the scale analysis of Section 4 starts with infinite velocity at $t = 0^+$ (see, e.g. the scaling law for u_1, equation (33)). This feature is a reflection of the Darcy flow model, that is, one result of neglecting the inertia of the fluid that seeps through the porous matrix. The effect of fluid inertia is felt precisely in the $t \to 0$ limit, when the fluid situated along the vertical midplane is subjected to a finite pressure step in the horizontal direction. In the $t \to 0$ limit, the pressure difference P of equation (27) can only be balanced by the horizontal fluid inertia ρu_p^2, where u_p is the scale of the horizontal fluid velocity through the pores. Relating u_p and the volume-averaged velocity scale through $u_p \sim u/\phi$, we conclude that in the $t \to 0$ limit the u scale is time independent, $u \to \phi(\Delta P/\rho)^{1/2}$. The time beyond which the Darcy-flow scale u_1 of equation (33) takes over is obtained by writing $u \sim u_1$, in other words

$$\phi\left(\frac{\Delta P}{\rho}\right)^{1/2} \sim \left(\frac{\sigma\alpha}{t} Ra\right)^{1/2}. \tag{80}$$

The resulting time scale is $t \sim \sigma K/(v\phi^2)$ or, in dimensionless terms

$$\hat{t} \sim \frac{K/H^2}{\phi^2\, Pr}. \tag{81}$$

This number can be considerably smaller than one, depending primarily on the smallness of K/H^2. In conclusion, the Darcy-flow scenario of Section 4 begins to apply starting with times t that are as small as the group identified in equation (81) above.

Acknowledgement—Both authors gratefully acknowledge the support received from the Electric Power Research Institute through contract No. RP 8006-4 under the management of Dr Jong H. Kim.

REFERENCES

1. C. E. Hickox and H. A. Watts, Steady thermal convection from a concentrated source in a porous medium, *J. Heat Transfer* **102,** 248–253 (1980).
2. C. E. Hickox, Thermal convection at low Rayleigh number from concentrated sources in porous media, *J. Heat Transfer* **103,** 232–236 (1981).
3. D. Poulikakos, On buoyancy induced heat and mass transfer from a concentrated source in an infinite porous medium, *Int. J. Heat Mass Transfer* **28,** 621–629 (1985).
4. S. E. Larson and D. Poulikakos, Double diffusion from a horizontal line source in an infinite porous medium, *Int. J. Heat Mass Transfer* **29,** 492–495 (1986).
5. D. Scott, R. Anderson and R. S. Figliola, Blockage of natural convection boundary layer flow in a multizone enclosure, paper presented at the AIAA/ASME Heat Transfer and Thermophysics Conference, Boston, Massachusetts, 2–4 June (1986).
6. P. Cheng, Heat transfer in geothermal systems, *Adv. Heat Transfer* **14,** 1–105 (1978).
7. P. Cheng, Geothermal heat transfer. In *Handbook of Heat Transfer* (Edited by W. M. Rohsenow, J. P. Hartnett and E. Ganic), 2nd Edn, Chap. 11. McGraw-Hill, New York (1985).
8. A. Bejan, *Convection Heat Transfer*, Chaps 9–11. Wiley, New York (1984).
9. S. V. Patankar, *Numerical Heat Transfer and Fluid Flow*. Hemisphere, Washington, D.C. (1980).
10. A. Bejan and C. L. Tien, Natural convection in a horizontal porous medium subjected to an end-to-end temperature difference, *J. Heat Transfer* **100,** 191–198 (1978); also **105,** 683–684 (1983).
11. K. L. Walker and G. M. Homsy, Convection in a porous cavity, *J. Fluid Mech.* **87,** 449–474 (1978).
12. D. Poulikakos and A. Bejan, Unsteady natural convection in a porous layer, *Physics Fluids* **26,** 1183–1191 (1983).

REPARTITION HORIZONTALE DES DEPOTS THERMIQUES ET CHIMIQUES DANS UN MILIEU POREUX

Résumé—On étudie analytiquement et numériquement la propagation horizontale, sous influence de la pesanteur, d'espèces thermiques et chimiques à travers un milieu poreux, saturé par un fluide. L'effet de flottement est dû à la fois aux gradients de température et de concentration. On montre que quand l'écoulement est piloté principalement par des gradients de température, l'approche d'un équilibre thermique éventuel peut se réaliser par deux voies distinctes, l'une dominée par des effets de convection (grand *Ra*) et l'autre dominée par la diffusion. Dans le premier régime, le milieu poreux atteint un état intermédiaire de stratification stable avant l'état final de température uniforme. On montre aussi que les mécanismes de migration d'espèces pour les écoulements pilotés par les gradients de température peuvent être rangés similairement selon l'importance de la convection de masse. Les tendances d'échelle et les prévisions obtenues analytiquement sont confirmées par des expériences numériques faites dans le domaine $10 < Ra < 10^3$, $0{,}01 < Le < 100$ et $1 < L/H < 4$. Les régimes distincts et les échelles de transfert de chaleur et de masse sont précisés pour les écoulements pilotés principalement par les gradients de concentration. Une solution analytique est développée pour le cas limite de couches infiniments peu profondes ($L/H \to \infty$).

DIE HORIZONTALE AUSBREITUNG VON WÄRME UND VON CHEMISCHEN SUBSTANZEN IN EINEM PORÖSEN MEDIUM

Zusammenfassung—Die auftriebsgesteuerte Ausbreitung von Wärme und von chemischen Substanzen in einem fluidgesättigten porösen Medium wird analytisch und numerisch untersucht. Der Auftrieb beruht sowohl auf Temperatur- als auch auf Konzentrationsgradienten. Für den Fall, daß die Strömung hauptsächlich durch Temperaturgradienten verursacht ist, wird gezeigt, daß die Annäherung an ein eventuelles thermisches Gleichgewicht entlang zweier verschiedener Pfade stattfinden kann. Der eine Weg wird durch Konvektionseinflüsse (hohe *Ra*-Zahlen), der andere durch Diffusion dominiert. Bei dem durch Konvektion dominierten Weg erreicht das poröse Medium zunächst einen Zwischenzustand mit stabiler Schichtung (horizontale Schichten) und dann erst den Endzustand mit gleichförmiger Temperatur. Es wird gezeigt, daß die Stofftransportprozesse ganz ähnlich verlaufen. Die analytischen Arbeiten werden durch umfangreiche numerische Experimente bestätigt, die in den Bereichen $10 < Ra < 10^3$, $0{,}01 < Le < 100$ und $1 < L/H < 4$ durchgeführt wurden. Eine geschlossene analytische Lösung wird für unendlich dünne Schichten ($L/H \to \infty$) entwickelt.

ГОРИЗОНТАЛЬНОЕ РАСПРЕДЕЛЕНИЕ ВЕЩЕСТВ В ПОРИСТОЙ СРЕДЕ ПРИ ТЕРМИЧЕСКОМ И ХИМИЧЕСКОМ ОСАЖДЕНИИ

Аннотация—Аналитически и численно исследуется обусловленное силами плавучести горизонтальное распределение тепла и химических веществ в насыщенной жидкостью пористой среде. Эффект плавучести имеет место благодаря как градиентам температуры, так и градиентам концентрации. Показано, что в первом случае тепловое равновесие может достигаться за счет действия двух четко выраженных механизмов: конвекции (при высоких числах Ra) и диффузии. Например, при конвективном режиме, прежде чем в пористой среде установится окончательное равномерное распределение температуры, в ней наблюдается промежуточное состояние устойчивой стратификации (горизонтальное расслоение). Кроме того показано, что процессы миграции веществ вместе с потоками, обусловленными градиентами температуры, можно классифицировать подобным же образом в зависимости от интенсивности конвекции. Полученные аналитические закономерности изменения масштабов величин и оценки подтверждены обширными численными экспериментами, проведенными в диапазонах $10 < Ra < 10^3$, $0{,}01 < Le < 100$ и $1 < L/H < 4$. Выявлены также четкие режимы и представлены соответствующие масштабы тепло-и массопереноса при свободноконвективных течениях, вызываемых градиентами концентрации.

Получено замкнутое аналитическое решение для бесконечно тонких слоев $L/H \to \infty$.